

# Tunable competing magnetic anisotropies and spin reconfigurations in ferrimagnetic $\text{Fe}_{100-x}\text{Gd}_x$ alloy films

A. Chanda<sup>✉</sup>, J. E. Shoup<sup>✉</sup>, N. Schulz, D. A. Arena<sup>✉</sup>, and H. Srikanth<sup>✉\*</sup>

Department of Physics, University of South Florida, Tampa, Florida 33620, USA



(Received 18 April 2021; revised 10 August 2021; accepted 23 August 2021; published 1 September 2021)

We report a comprehensive study of the temperature evolution of in-plane (IP) and out-of-plane (OOP) effective magnetic anisotropies in compensated ferrimagnetic  $\text{Fe}_{100-x}\text{Gd}_x$  alloy films by employing direct current magnetometry and radiofrequency (RF) transverse susceptibility (TS) measurements. We suggest that our  $\text{Fe}_{100-x}\text{Gd}_x$  system is chemically inhomogeneous and phase segregates into Fe- and Gd-enriched regions. Our IP and OOP magnetometry results indicate that the system undergoes a temperature-driven transformation from an IP-spin-configuration-dominated state to an OOP-spin-configuration-dominated state below a certain temperature (spin reorientation temperature). A two-step reversal behavior emerges in the OOP  $M(H)$  loop near compensation, which we attribute to the sequential magnetization reversals of Fe- and Gd-enriched domains. Field-induced spin-flop transitions were also observed near the compensation. Our RF TS measurements indicate that the effective magnetic anisotropy for the OOP configuration dominates over that for the IP configuration below a certain spin reorientation temperature. Both IP and OOP anisotropy fields determined from our TS measurement exhibit a minimum around the compensation temperature, which has been explained in the framework of the Stoner-Wohlfarth model.

DOI: [10.1103/PhysRevB.104.094404](https://doi.org/10.1103/PhysRevB.104.094404)

## I. INTRODUCTION

Antiferromagnets serve as a promising alternative to ferromagnets due to their potential for spintronic applications, as their highly stable antiparallel spin configuration produces negligible stray fields. Particularly interesting are ferrimagnetic materials, as they bring together some of the compelling features of both ferromagnets and antiferromagnets. Recently, there has been a resurgence of interest in rare earth (RE)-transition metal (TM) ferrimagnetic thin films with perpendicular magnetic anisotropy (PMA) because of their prospects for wide-ranging magneto-optical [1] and spintronic applications including ultrafast light-controlled magnetic switching [2,3], heat-assisted magnetic recording/thermomagnetic switching [4–6], spin-orbit torque-driven magnetization switching [7–9], multilevel current-induced switching [10], terahertz emission [11], and even for hosting stable topological spin textures [12,13]. This fascinating class of materials has been well known for decades due to its intriguing magnetic properties including PMA [14–16]. Another remarkable characteristic of the RE-TM family is the temperature-tuned spin reorientation transition stemming from the competition between PMA and in-plane (IP) shape anisotropy [17,18]. Several mechanisms have been proposed in the past few years to attempt to understand the physical origin of PMA in amorphous RE-TM ferrimagnetic films, namely, the RE single-ion anisotropy [19], exchange anisotropy [20], magnetoelasticity-induced bond-orientation anisotropy [21], pair ordering originating from magnetic dipole

interactions between anisotropically distributed atomic moment pairs [22], anisotropic pair-pair correlations [23], and most recently, nanoscale chemical phase segregation [24].

Like other members of the RE-TM-based ferrimagnetic films, the FeGd amorphous ferrimagnetic films also provide flexibility to tune the saturation magnetization, coercive field, magnetic anisotropy, and compensation temperature by varying the chemical composition [25,26]. In addition, the FeGd amorphous films possess a reasonably large magnetic moment in both sublattices and exhibit excellent laser-induced composition temperature switching, which makes this system a potential candidate for magneto-optical recording [27]. While other members of the RE-TM family, for example, Tb-based RE-TM systems, exhibit weak exchange coupling between the Tb and TM sublattices, giving rise to a broad orientational distribution of the RE moment often termed *sperrimagnetism*, the Gd moments are strongly exchange coupled to the Fe moments in FeGd systems, giving rise to a stable collinear ferrimagnetic spin configuration at low fields [28]. Moreover, compared with the RE-Co-based films, e.g., TbCo, the saturation magnetization of FeGd amorphous films is weakly dependent on the argon pressure [29]. All these features make the  $\text{Fe}_{100-x}\text{Gd}_x$  amorphous films particularly attractive from both fundamental and application points of view. Magnetic properties of single-layer  $\text{Fe}_{100-x}\text{Gd}_x$  alloy films [30–32] as well as Fe/Gd multilayer heterostructures [33,34] have been extensively investigated over the past few years. Depending on the temperature and applied magnetic field strength, both single and multilayer films exhibit exotic magnetic phases. Since the ordering temperatures of Fe and Gd are significantly different ( $T_C^{\text{Fe}} \approx 1043$  K and  $T_C^{\text{Gd}} \approx 293$  K), the ordering temperature of  $\text{Fe}_{100-x}\text{Gd}_x$

\*sharihar@usf.edu

alloy and Fe/Gd multilayer films lies between  $T_C^{\text{Fe}}$  and  $T_C^{\text{Gd}}$  because of strong exchange coupling between Fe and Gd sublattices. However, upon lowering temperature, the magnetization of the Gd sublattice increases more steeply than the Fe sublattice; because of this, there exists a compensation temperature ( $T_{\text{Comp}}$ ) at which the Fe-sublattice magnetization ( $M_{\text{Fe}}$ ) cancels out the Gd-sublattice magnetization ( $M_{\text{Gd}}$ ). It is known that  $M_{\text{Fe}} > M_{\text{Gd}}$  for  $T > T_{\text{Comp}}$ , and  $M_{\text{Gd}} > M_{\text{Fe}}$  for  $T < T_{\text{Comp}}$  [34]. According to the  $(H, T)$  phase diagram constructed by Camley and Tilley [35] for Fe/Gd multilayers, when the applied field ( $H_{\text{DC}}$ ) strength is lower than a certain critical value, the system transforms from the Fe-aligned state ( $M_{\text{Fe}} \parallel H_{\text{DC}}$ ) for  $T > T_{\text{Comp}}$  to the Gd-aligned state ( $M_{\text{Gd}} \parallel H_{\text{DC}}$ ) for  $T < T_{\text{Comp}}$ . If  $H_{\text{DC}}$  exceeds the critical value, the collinear Gd-aligned (Fe-aligned) state for  $T < T_{\text{Comp}}$  ( $T > T_{\text{Comp}}$ ) transforms into a noncollinear metastable state, also known as the *twisted state* [35]. The occurrence of such a field-induced phase transformation suggests the existence of spin-flop (SF) transition in these systems [36]. The emergence of such SF state has also been observed in  $\text{Fe}_{100-x}\text{Gd}_x$  amorphous films via Hall measurements [37]. Moreover, the  $\text{Fe}_{100-x}\text{Gd}_x$  amorphous films exhibit excellent PMA for a certain composition range [38–40], the origin of which cannot be explained by a pair-ordering mechanism, as Gd does not possess single-ion magnetic anisotropy [41]. Most recently, by exploiting superconducting quantum interference device vibrating sample magnetometry (VSM), scanning transmission x-ray microscopy, and scanning transmission electron microscopy equipped with energy-dispersive x-ray spectroscopy (EDS), Kirk *et al.* [24] showed the presence of nanoscale chemical phase segregation in the FeGd amorphous films; this leads to the formation of Gd-enriched columnar domain structures with out-of-plane (OOP) anisotropy surrounded by Fe-enriched regions with IP anisotropy. They showed that it is possible to tune the competing anisotropies by changing the film thickness, which in turn tailors the spin reorientation transition. To better understand the PMA and spin reorientation temperature window in  $\text{Fe}_{100-x}\text{Gd}_x$  amorphous films and to manipulate these properties for efficient magneto-optical and spintronic applications, a comprehensive study of the temperature profile of both IP and OOP magnetic anisotropy is indispensable.

In this paper, we have thoroughly investigated the magnetic properties of single-layer ferrimagnetic amorphous thin films of  $\text{Fe}_{100-x}\text{Gd}_x$  ( $22.8 \leq x \leq 26.2$ ) by utilizing VSM and tunnel diode oscillator (TDO)-based radiofrequency (RF) transverse susceptibility (TS) measurements. RF TS is a well-known ultrasensitive technique to precisely determine the effective magnetic anisotropy. It was shown that the compensation temperature can be shifted to a higher temperature by increasing the Gd concentration, which was confirmed by VSM measurements. From IP and OOP magnetometry measurements, we observed that the system undergoes a temperature-driven transformation from an IP-spin-configuration-dominated state to an OOP-spin-configuration-dominated state below a certain temperature (spin reorientation temperature). From the TS measurements performed in both IP and OOP configurations, we have demonstrated that the effective magnetic anisotropy is higher

for the OOP configuration than the IP configuration below the spin reorientation transition, which strongly agrees with our magnetometry results as well as previous predictions [24,38–40] of PMA in these amorphous  $\text{Fe}_{100-x}\text{Gd}_x$  films. Both IP and OOP anisotropy fields determined from our TS measurement exhibit a minimum around  $T_{\text{Comp}}$ , which has been explained in the framework of the Stoner-Wohlfarth (SW) model.

## II. EXPERIMENTAL

The samples were grown on a silicon substrate using a combination of direct current (DC) and RF magnetron sputtering at room temperature in an ultrahigh vacuum deposition chamber with a base pressure of  $4 \times 10^{-9}$  Torr. All samples have the same nominal structure: substrate/SiO<sub>2</sub>(3 nm)/Ta(8 nm)/ $\text{Fe}_{100-x}\text{Gd}_x$ (80 nm)/Ta(6 nm). The Gd concentration ( $x$ ) was varied with the following concentrations:  $x = 22.8, 24.3, 25.3$ , and  $26.2$  (%) and designated as samples A, B, C, and D, respectively. The  $\text{Fe}_{100-x}\text{Gd}_x$  layers were grown by cosputtering from pure Fe and Gd targets and changing the power of the Gd gun to achieve the variation in the concentration. The composition of the samples was measured using EDS and had a standard deviation of  $<1\%$ . To obtain the structural profile of the samples, we performed low-angle x-ray reflectivity (XRR) scans across an angular range of  $0^\circ$  to  $\sim 5^\circ$  [42]. Our XRR results indicate that the  $\text{Fe}_{100-x}\text{Gd}_x$  films were  $\approx 750 \pm 20$  Å thick, and the Ta cap and seed layers were  $60 \pm 10$  and  $75 \pm 5$  Å thick. Interfacial roughness at the bottom Ta/ $\text{Fe}_{100-x}\text{Gd}_x$  was  $6 \pm 2$  Å, and the interface between the Ta cap and the  $\text{Fe}_{100-x}\text{Gd}_x$  layer was  $33 \pm 10$  Å. High-angle x-ray diffraction confirmed the amorphous nature of our films [42].

The IP and OOP static magnetic characterization of the samples were performed using VSM attached to the physical property measurement system (PPMS; Quantum Design, Inc., USA). TS measurements were performed by making use of a custom-built self-resonant TDO circuit with a resonance frequency of  $\approx 12$  MHz and a sensitivity of  $\approx 10$  Hz. The film was placed inside an inductor (L) coil of the inductor-capacitor (LC) tank circuit and incorporated into the PPMS in such a manner that the RF magnetic field ( $H_{\text{RF}}$ ) generated inside the coil was oriented along the plane of the film surface but transverse to the direction of the external DC magnetic field ( $H_{\text{DC}}$ ) produced by the superconducting magnet of the PPMS. The remaining components of the TDO circuit were accommodated outside the PPMS. Here, the PPMS served as a platform to sweep the DC magnetic field and temperature. Note that the geometry of our experimental setup allows both IP ( $H_{\text{DC}} \parallel$  film surface) and OOP ( $H_{\text{DC}} \perp$  film surface) configurations;  $H_{\text{DC}} \perp H_{\text{RF}}$  for both configurations. The magnetic field dependence of TS at a fixed temperature was performed by recording the change in the resonant frequency of the LC tank circuit as the  $H_{\text{DC}}$  was swept from positive to negative saturation and then back to positive saturation. We restricted the TS measurements to the range of  $40 \text{ K} \leq T \leq 300 \text{ K}$ , as it was difficult to stabilize the coil temperature (and hence the sample temperature)  $< 40 \text{ K}$ .

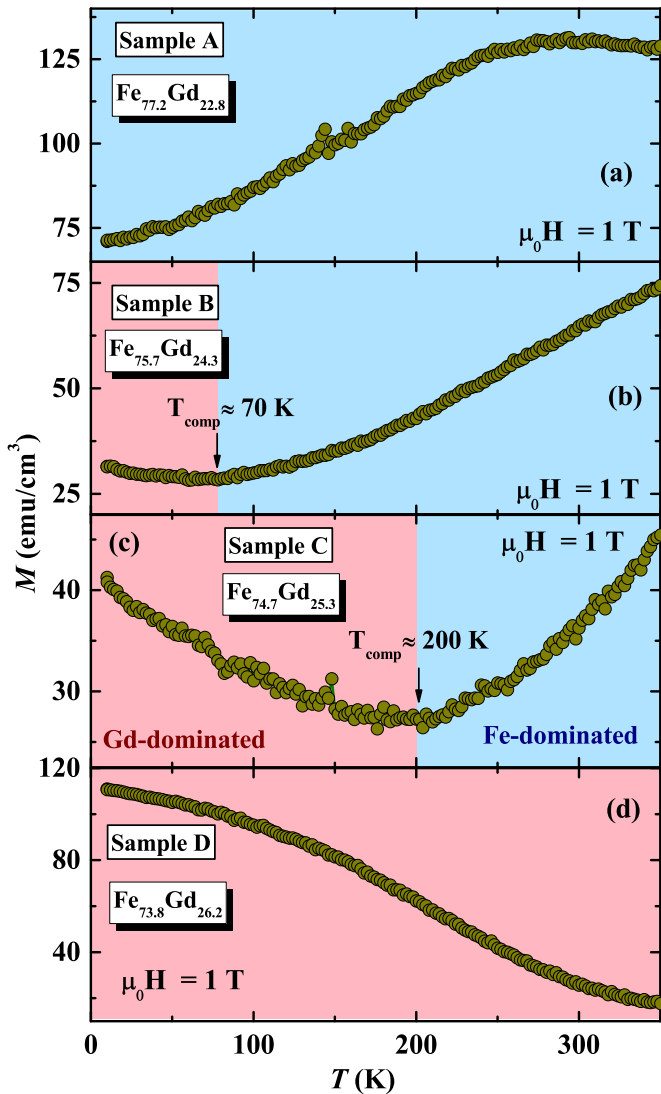


FIG. 1. (a)–(d) Temperature dependence of in-plane (IP) magnetization  $M(T)$  of the  $\text{Fe}_{100-x}\text{Gd}_x$  films with different Gd concentrations (samples A–D, respectively) measured in a magnetic field of  $\mu_0 H = 1$  T in the field-cooled cooling mode.

### III. RESULTS

#### A. Temperature and magnetic field dependence of magnetization

Figures 1(a)–1(d) display the temperature dependence of the IP magnetization  $M(T)$  of the  $\text{Fe}_{100-x}\text{Gd}_x$  films with different Gd concentrations measured in a magnetic field of  $\mu_0 H = 1$  T in the temperature range  $10 \text{ K} \leq T \leq 350 \text{ K}$ . The  $M(T)$  of sample A (lowest Gd concentration) decreases almost monotonically down to the lowest temperature. On the other hand, the  $M(T)$  of sample B also shows a gradual decrease upon cooling, but a broad minimum appears  $\sim 70 \text{ K}$ , which we identify as the compensation temperature ( $T_{\text{Comp}}$ ). The compensation is more prominent for sample C, and it occurs at a higher temperature ( $T_{\text{Comp}} = 200 \text{ K}$ ) than sample B; therefore,  $T_{\text{Comp}}$  moves to a higher temperature upon increasing Gd concentration. For sample D with the highest Gd concentration, the compensation point is above the measured

range, and hence, the  $M(T)$  gradually increases upon cooling down to the lowest temperature.

In the main panels of Figs. 2(a)–2(d), we compared the IP and OOP  $M(H)$  loops at  $T = 300 \text{ K}$  for the films A–D, respectively. A diamagnetic contribution from the  $\text{SiO}_2$  substrate was subtracted from all  $M(H)$  loops. Note that the magnetization of the saturated ferrimagnetic macrospins is indicated as the saturation magnetization  $M_S$  throughout the paper. Sample A shows nearly saturated square-shaped hysteresis loops for both IP and OOP configurations. A closer look [inset of Fig. 2(a)] reveals that the OOP  $M(H)$  first shows a steep jump near the zero field followed by a gradual evolution toward the opposite saturation. Such a behavior of  $M(H)$  was previously observed in Fe/Cr/Gd superlattices with Cr thickness  $> 10 \text{ \AA}$ , which was attributed to independent magnetization reversals of noninteracting Fe and Gd sublattice magnetizations with different coercive fields [43]. For samples B–D, the IP  $M(H)$  loop becomes elongated with an increase in the saturation field limit, whereas the OOP  $M(H)$  loop exhibits a nearly square-shaped hysteresis loop with a noticeable and consistent increase in coercivity upon increasing Gd concentration, which is evident from the insets of Figs. 2(b)–2(d), respectively. For samples A–C, the magnetization value at  $\mu_0 H = 1 \text{ T}$  is higher for the IP configuration than the OOP configuration. For sample D, the magnetization value at  $\mu_0 H = 1 \text{ T}$  for the OOP  $M(H)$  loop is slightly higher than that for the IP  $M(H)$  loop. In the main panel of Figs. 2(e)–2(h), we compared the IP and OOP  $M(H)$  loops at  $T = 10 \text{ K}$  for samples A–D. The IP  $M(H)$  loops are more elongated in shape than  $T = 300 \text{ K}$  for samples A–D, whereas the OOP  $M(H)$  loops are nearly square-shaped for all samples [see the insets of Figs. 2(e)–2(h) for details]. Hence, the effective easy direction of magnetization is mostly oriented along the OOP direction at  $T = 10 \text{ K}$  for the films A–D. Moreover, a smaller to negligible difference in the magnetization value at  $\mu_0 H = 1 \text{ T}$  between the IP and OOP configurations is evident for samples A–C. Moreover, the OOP  $M(H)$  loops at  $T = 10 \text{ K}$  exhibit distinct shapes in different samples. While samples A and D exhibit a square OOP hysteresis loop with a single-step reversal, two-step magnetization reversals are observed in samples B and C. This two-step magnetization reversal behavior is more prominent in sample B than sample C. Moreover, it is also evident that the coercive field decreases gradually with increasing Gd concentration at  $T = 10 \text{ K}$ , which is more prominent from the insets of Figs. 2(e)–2(h).

To understand the evolution of the two-step reversal feature in the OOP  $M(H)$ , we have investigated the hysteresis loops for all our samples at different temperatures. Figures 3(a)–3(d) depict the plots of the OOP  $M(H)$  loops in the temperature range  $10 \leq T \leq 300 \text{ K}$  for samples A–D, respectively. The OOP  $M(H)$  loops for both samples A and D exhibit a mostly square shape for all temperatures. While sample A shows a significant increase in coercivity with decreasing temperature, a monotonic decrease in coercivity upon reducing the temperature is evident for sample D. However, samples B and C show anomalous temperature evolutions of the OOP  $M(H)$  loops. For sample B, the  $M(H)$  loop exhibits a single step reversal for  $T \geq 200 \text{ K}$ , but the two-step magnetization reversal starts appearing for  $T \leq 150 \text{ K}$ , and it becomes stronger close to the compensation point. At  $T = 100 \text{ K}$ , a notable

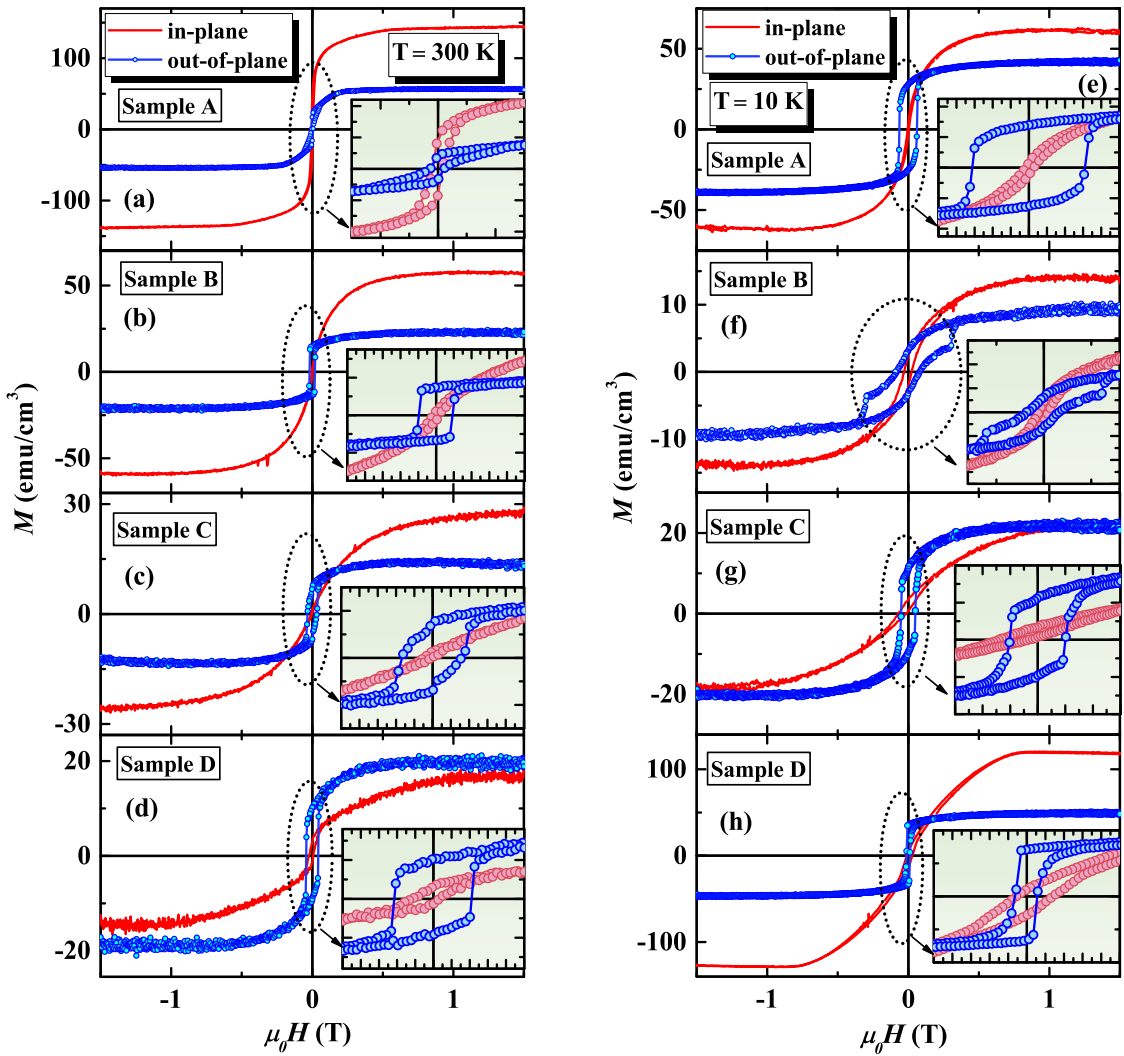


FIG. 2. (a)–(d) In-plane (IP) and out-of-plane (OOP)  $M(H)$  loops at  $T = 300$  K for the films A–D, respectively, and (e)–(h) IP and OOP  $M(H)$  measured at  $T = 10$  K for the same samples; insets show expanded view of the low-field hysteresis behavior of the  $M(H)$  loops.

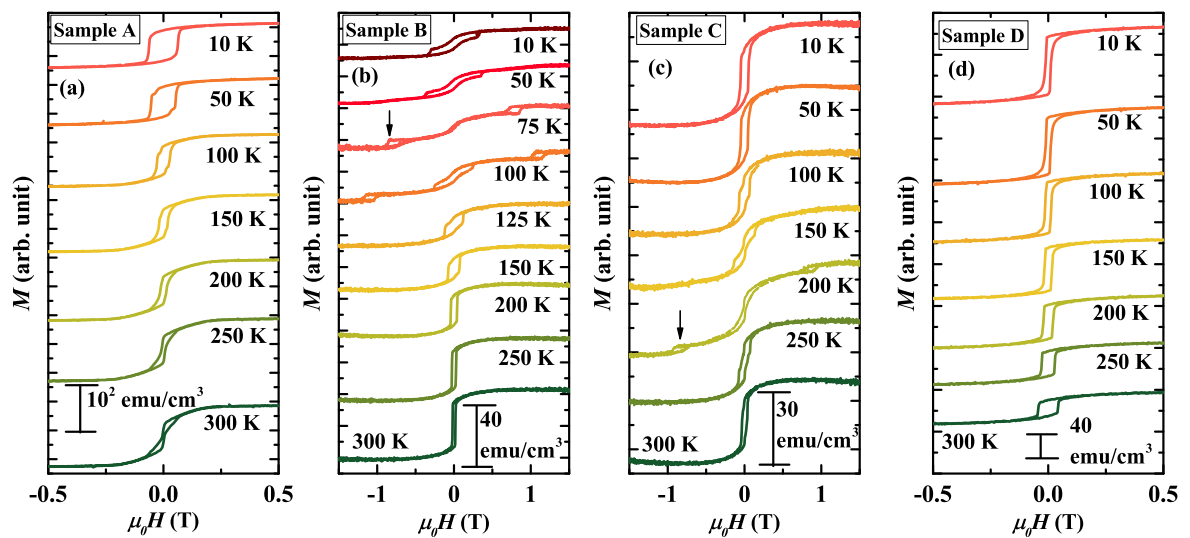


FIG. 3. (a)–(d) The out-of-plane (OOP)  $M(H)$  loops in the temperature range  $10 \leq T \leq 300$  K for samples A–D, respectively.

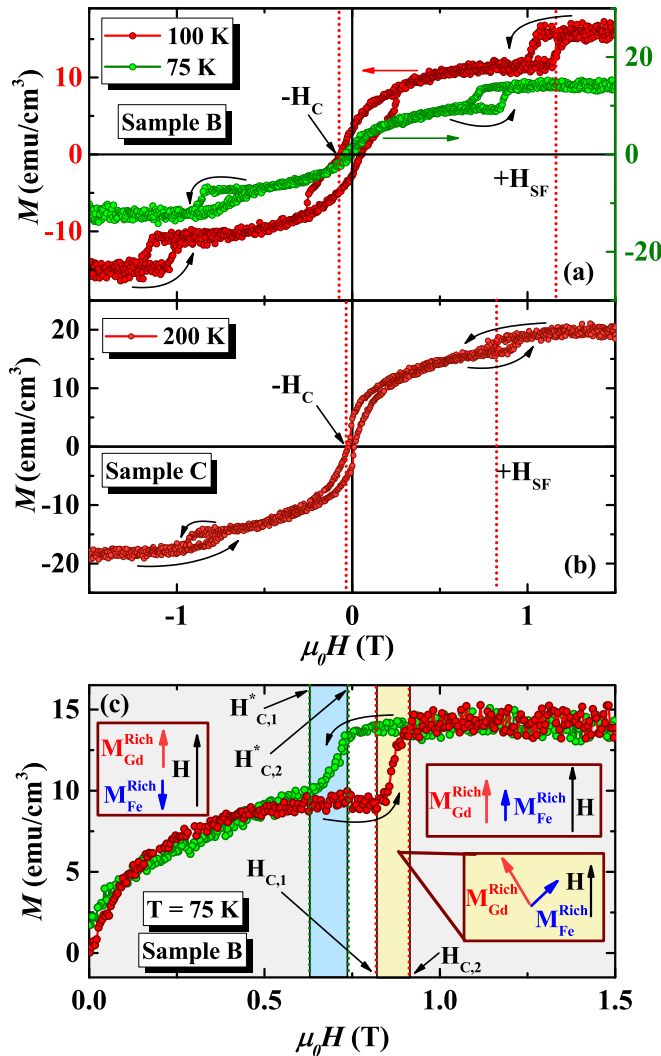


FIG. 4. (a) Out-of-plane (OOP)  $M(H)$  loops at  $T = 75$  and  $100$  K for sample B, (b) OOP  $M(H)$  at  $T = 200$  K for sample C, and (c) expanded view of OOP  $M(H)$  loop for sample B at  $T = 75$  K for better visibility of the spin-flop (SF) transition. The SF transition and coercive fields are indicated by  $H_{\text{SF}}$  and  $H_C$ , respectively, in the figure.

feature appears in the  $M(H)$  loop: an additional magnetization switching with a minor hysteresis loop around  $\mu_0 H_{\text{SF}} \approx 1$  T, which is reproducible for the reverse field cycle. For clarity, the OOP  $M(H)$  loops at  $T = 75$  and  $100$  K for sample B are shown separately in Fig. 4(a). Interestingly, this feature occurs at a lower field strength ( $\mu_0 H_{\text{SF}} \approx 0.8$  T) around the compensation point ( $T = 75$  K), but the two-step magnetization reversal disappears, and the  $M(H)$  loop shows significantly lower coercivity. As the temperature is further reduced below compensation, the magnetization switching behavior at  $\mu_0 H_{\text{SF}}$  disappears, but the two-step magnetization reversal reappears. Similar temperature evolution of the OOP  $M(H)$  was also observed in sample C around the compensation temperature  $T_{\text{Comp}} = 200$  K. For clarity, the OOP  $M(H)$  at  $T = 200$  K is shown separately in Fig. 4(b), which exhibits a magnetization switching accompanied by a minor hysteresis loop around  $\mu_0 H_{\text{SF}} \approx 0.8$  T, as in sample B. As observed in sample B,

this feature at  $\mu_0 H_{\text{SF}}$  disappears below the compensation. Although the two-step magnetization reversal reappears below compensation, it fades away below  $T = 100$  K.

In Figs. 5(a)–5(d), we show the temperature dependence of saturation magnetization ( $M_S$ ) normalized with respect to its value at  $T = 300$  K ( $M_S/M_S^{300\text{K}}$ ) on the left vertical scale and the ratio of remanent magnetization ( $M_R$ ) and  $M_S$  on the right vertical scale obtained from the OOP  $M(H)$  loops for the samples A–D. The ratio  $M_R/M_S$  determines the squareness of the hysteresis loop and hence an important parameter to understand the behavior of magnetic anisotropy. For sample A, which does not show any compensation,  $M_S/M_S^{300\text{K}}$  initially decreases smoothly up to  $150$  K and then abruptly decreases down to the lowest temperature, whereas  $M_R/M_S$  increases smoothly with decreasing temperature along with a slope change  $\sim 150$  K. We believe that steep enhancement of Gd-sublattice magnetization for  $T \leq 150$  K is responsible for this behavior, which also hints that the easy direction of magnetization is tilting toward the OOP orientation. In a sharp contrast to sample A,  $M_S/M_S^{300\text{K}}$  and  $M_R/M_S$  for both samples B and C exhibit minima around their compensation point, which is followed by an increase in both these parameters, indicating a strong influence of magnetic anisotropy on the magnetic behavior of these samples around their compensation. In the case of sample D, for which compensation is expected at a higher temperature than both samples B and C, both  $M_S/M_S^{300\text{K}}$  and  $M_R/M_S$  smoothly increase with decreasing temperature, which is consistent with a sample with a high compensation temperature. We have also shown the temperature profiles of the coercive field for the OOP configuration ( $H_C^{\text{OOP}}$ ) for the samples A–D in Figs. 5(e)–5(h), respectively. While  $H_C^{\text{OOP}}$  for sample A smoothly increases with decreasing temperature, for samples B and C,  $H_C^{\text{OOP}}$  exhibits a sharp minimum around  $T = T_{\text{Comp}}$  for those samples, respectively. For both samples B and C,  $H_C^{\text{OOP}}$  decreases steeply as the temperature moves away from the compensation point. Such a behavior strongly suggests that a drastic change in anisotropy energy occurs in the vicinity of the compensation point in these films.

## B. TS and temperature dependence of effective magnetic anisotropy

To investigate the behavior of the effective magnetic anisotropy of  $\text{Fe}_{100-x}\text{Gd}_x$  films under the application of IP and OOP DC bias fields, we performed TS measurements by utilizing a TDO-based self-resonant RF technique. TS is an extremely sensitive tool to precisely determine the dynamic magnetic response of the material to a small and fixed amplitude RF ( $f = 12\text{MHz}$ ) perturbing magnetic field ( $H_{\text{RF}} \sim 10\text{ Oe}$ ) applied perpendicular to a static magnetic field ( $H_{\text{DC}}$ ) [44]. The self-resonant circuit consists of an LC tank circuit, and the sample is placed inside the inductor. An application of a DC magnetic field induces a shift in the resonance frequency of the LC tank circuit which provides a direct measurement of the change in inductance and hence the susceptibility of the sample. In the framework of the SW model, if  $H_{\text{DC}}$  is scanned from positive to negative saturation (and vice versa), the TS for a single-domain particle with uniaxial anisotropy shows sharp peaks at the anisotropy fields

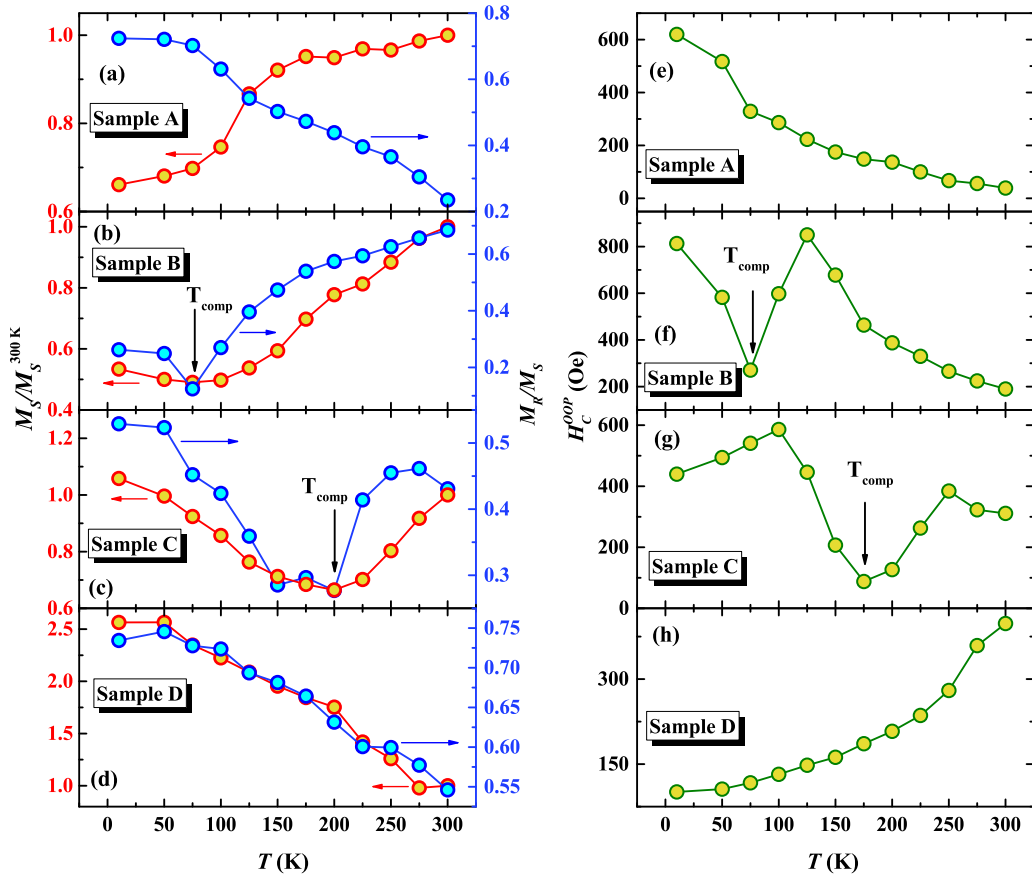


FIG. 5. (a)–(d) Temperature dependence of saturation magnetization ( $M_S$ ) normalized with respect to its value at  $T = 300\text{ K}$  ( $M_S/M_S^{300\text{ K}}$ ) on the left y scale and the ratio of remanent magnetization ( $M_R$ ) and  $M_S$  on the right y scale obtained from the out-of-plane (OOP)  $M(H)$  loops for the samples A–D, respectively. (e)–(h) Coercivity ( $H_C$ ) of the OOP  $M(H)$  loops as a function of temperature for samples A–D, respectively. Note that the magnetization of the saturated ferrimagnetic macrospins is indicated as the saturation magnetization  $M_S$  throughout the paper.

$H_{\text{DC}} = \pm H_K$ , which is also known as the Aharoni singularity [45]. However, for a system with randomly dispersed magnetic easy axes, the field dependence of TS usually exhibits cusp(s) at the effective anisotropy field(s)  $H_{\text{DC}} = \pm H_K^{\text{eff}}$ . Figure 6(a) represents the three-dimensional polar representation of different orientations of the magnetization vector ( $M_S$ ), DC, and RF magnetic fields relative to the magnetic easy axis of a single-domain particle with uniaxial magnetic anisotropy fulfilling the experimental conditions of a typical TS measurement in the framework of the SW model. Considering the diagram, if  $H_{\text{DC}}$  and  $H_{\text{RF}}$  are applied along the  $z$  and  $x$  axes respectively,  $(\theta_K, \phi_K)$  and  $(\theta_M, \phi_M)$  are the (polar, azimuthal) angles of the uniaxial anisotropy axis and the saturation magnetization  $M_S$ , respectively, the TS can be expressed as [45]

$$\frac{\chi_T}{\chi_0} = \frac{3}{2} \left[ \cos^2 \phi_K \frac{\cos^2 \theta_M}{h \cos \theta_M + \cos 2(\theta_M - \theta_K)} + \sin^2 \phi_K \frac{\sin(\theta_K - \theta_M)}{h \sin \theta_K} \right], \quad (1)$$

where  $h$  is the reduced applied field ( $h = \frac{H_{\text{DC}} M_S}{2K} = \frac{H_{\text{DC}}}{H_K}$ ), and  $K$  is the uniaxial anisotropy energy density. For randomly oriented anisotropy axes, the average TS can be expressed

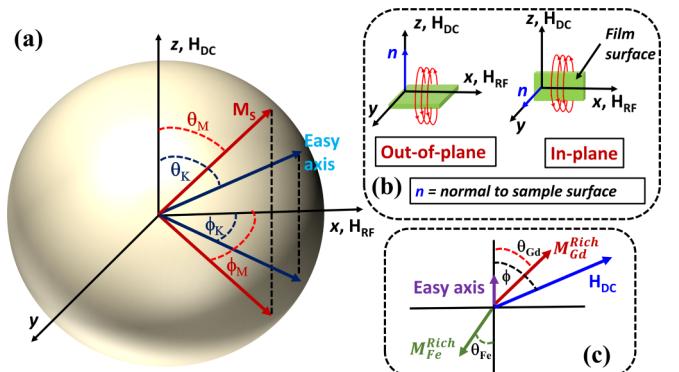


FIG. 6. (a) Three-dimensional polar representation of different orientations of the magnetization vector ( $M_S$ ), direct current (DC), and radiofrequency (RF) magnetic fields relative to the magnetic easy axis of a single-domain particle with uniaxial magnetic anisotropy fulfilling the experimental conditions of a typical transverse susceptibility (TS) measurement, (b) schematic of our TS measurement geometry for in-plane (IP) and out-of-plane (OOP) configurations, and (c) schematic representation of different orientations of Gd sub-lattice magnetization ( $M_{\text{Gd}}$ ) and Fe sublattice magnetization ( $M_{\text{Fe}}$ ) relative to the applied bias field ( $H_{\text{DC}}$ ).

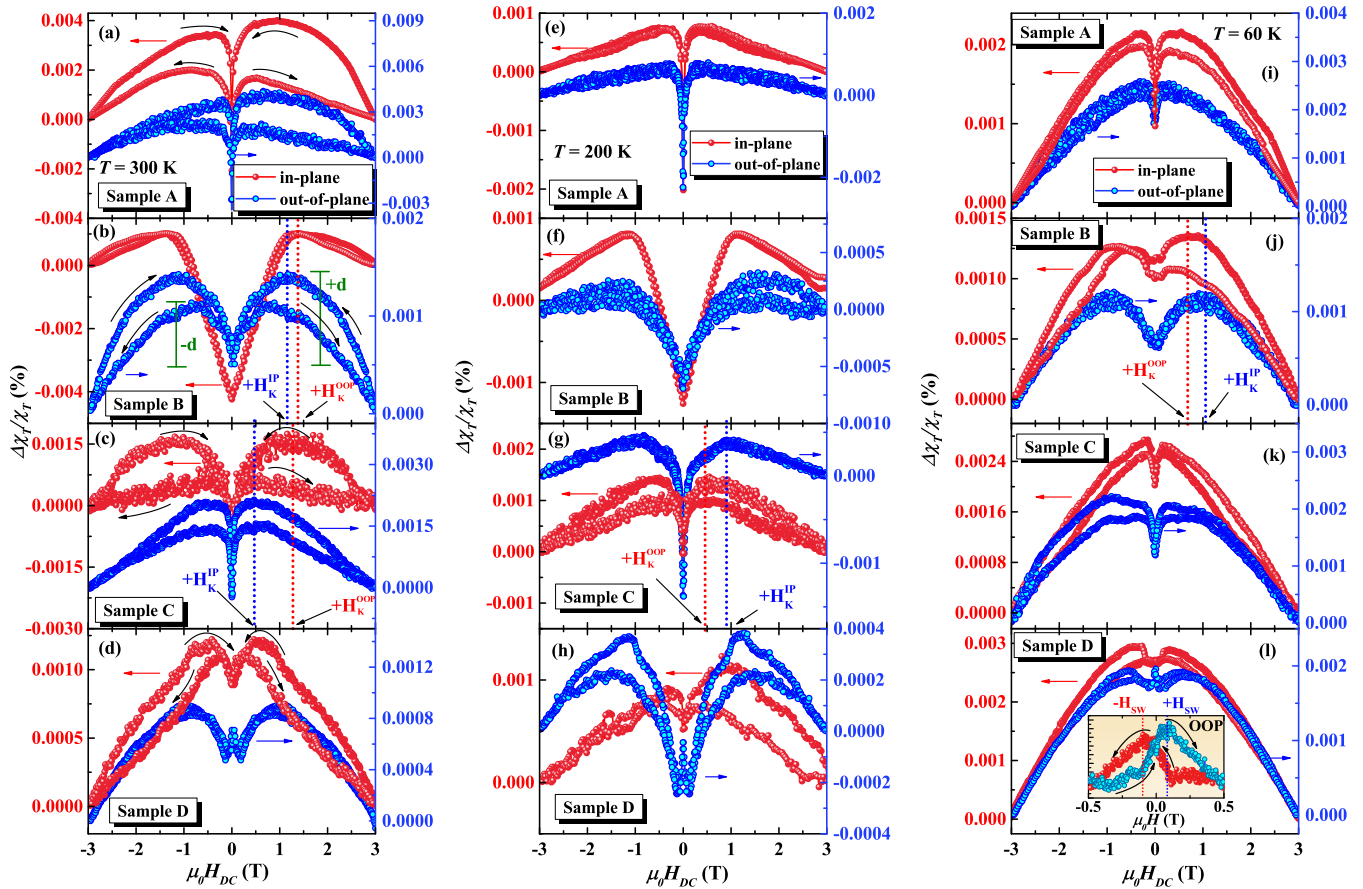


FIG. 7. In-plane (IP; left y scale) and out-of-plane (OOP; right y scale) transverse susceptibility (TS) data for samples A–D, respectively, for bipolar field scans ( $+H_{\text{DC}}^{\text{sat}} \rightarrow -H_{\text{DC}}^{\text{sat}} \rightarrow +H_{\text{DC}}^{\text{sat}}$ ) at (a)–(d)  $T = 300$  K, (e)–(h)  $T = 200$  K (close to the compensation for sample C), and (i)–(l)  $T = 60$  K (close to the compensation for sample B).

as [45]

$$\left\langle \frac{\chi_T}{\chi_0} \right\rangle = \frac{3}{4} \int_0^{\pi/2} \left[ \frac{\cos^2 \theta_M}{h \cos \theta_M + \cos 2(\theta_M - \theta_K)} \right. \\ \left. + \frac{\sin(\theta_K - \theta_M)}{h \sin \theta_K} \right] \sin \theta_K d\theta_K. \quad (2)$$

Equation (2) can be used to numerically calculate the average TS for single-domain SW particles with randomly oriented anisotropy axes. The DC bias field-dependent TS for such systems exhibits sharp peaks at the anisotropy fields  $\pm H_K$  as well as at the switching field ( $H_{SW}$ ). However, for a system consisting of different regions with distinct anisotropy energy density, the TS probes the effective anisotropy field  $H_K^{\text{eff}}$ , and the DC bias field-dependent TS exhibits broad maxima centering around  $\pm H_K^{\text{eff}}$ . In that case, it is essential to introduce the magnetic anisotropy field dispersion in the calculations by incorporating a log-normal distribution of the anisotropy fields in the Eq. (2) with a mean value of  $\approx H_K^{\text{eff}}$  as [46,47].

$$\begin{aligned} \left\langle \widetilde{\frac{\chi_T}{\chi_0}(H_{\text{DC}})} \right\rangle &= \int_0^{\infty} \frac{1}{\sqrt{2\pi}\sigma H_{\text{K}}} \left\langle \frac{\chi_T}{\chi_0} \left( \frac{H_{\text{DC}}}{H_{\text{K}}} \right) \right\rangle \\ &\times \exp \left\{ -\frac{1}{2} \left[ \frac{\ln \left( \frac{H_{\text{K}}}{H_{\text{eff}}} \right)}{\sigma} \right]^2 \right\} dH_{\text{K}}, \quad (3) \end{aligned}$$

where  $\sigma$  represents the standard deviation of the quantity  $\frac{H_K}{H_K^{\text{eff}}}$ . The standard deviation of the anisotropy field can thus be expressed as  $\sigma_{H_K} = \sigma H_K^{\text{eff}}$ . Numerical calculations of the TS using Eq. (3) showed that, for unipolar field scans ( $+H_{\text{DC}}^{\text{sat}} \rightarrow -H_{\text{DC}}^{\text{sat}}$ ), (a) the peaks associated with the effective anisotropy fields ( $\pm H_K^{\text{eff}}$ ) are significantly broadened, and (b) the peak heights at  $+H_K^{\text{eff}}$  and  $-H_K^{\text{eff}}$  are asymmetric with respect to the zero field in the presence of anisotropy dispersion. These observations were also confirmed experimentally [46,47].

We have conducted the TS measurements on our  $\text{Fe}_{100-x}\text{Gd}_x$  films at various temperatures in the range  $40 \text{ K} \leq T \leq 300 \text{ K}$  by saturating them at  $\mu_0 H_{\text{DC}}^{\text{sat}} = 3 \text{ T}$  for two different orientations of  $H_{\text{DC}}$ : IP ( $H_{\text{DC}}$  lies along the film surface) and OOP ( $H_{\text{DC}}$  is perpendicular to the film surface). Note that  $H_{\text{DC}} \perp H_{\text{RF}}$  for both configurations. The schematic of our TS measurement geometry for IP and OOP configurations is shown in Fig. 6(b). Since the TS data were directly obtained from the shift in the resonance frequency of the self-resonant LC tank circuit, we show all TSs in this paper as percentage change, which is defined as  $\frac{\Delta\chi_T}{\chi_T} (\%) = \frac{\chi_T(H_{\text{DC}}) - \chi_T(H_{\text{DC}}^{\text{sat}})}{\chi_T(H_{\text{DC}}^{\text{sat}})} \times 100$ , where  $\chi_T(H_{\text{DC}}^{\text{sat}})$  is the value of the TS at the saturation field ( $\mu_0 H_{\text{DC}}^{\text{sat}}$ ).

Figures 7(a)–7(d) compare the IP and OOP TS data for samples A–D for bipolar field scans ( $+H_{\text{DC}}^{\text{sat}} \rightarrow -H_{\text{DC}}^{\text{sat}} \rightarrow +H_{\text{DC}}^{\text{sat}}$ ) at  $T = 300\text{ K}$ . For all samples, the TS exhibits a broad

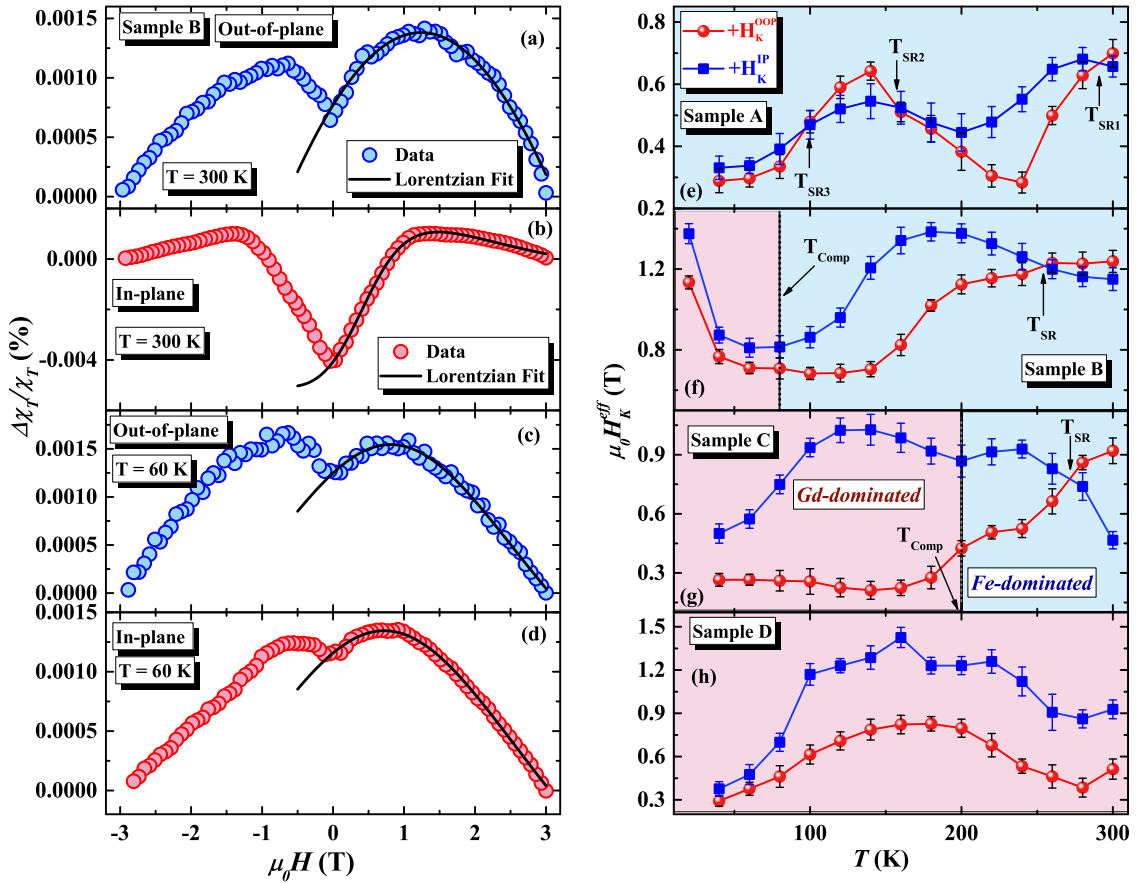


FIG. 8. Lorentzian fits to the out-of-plane (OOP) and in-plane (IP) transverse susceptibility (TS) line shapes for sample B at (a) and (b)  $T = 300$  K and (c) and (d)  $T = 60$  K. Temperature dependence of IP anisotropy field ( $+H_K^{IP}$ ) and OOP anisotropy field ( $+H_K^{OOP}$ ) for the samples A–D are shown in (e)–(h), respectively.

maximum centering at the effective anisotropy fields  $\pm H_K^{\text{eff}}$  for both IP and OOP orientations. Additionally, significant asymmetry in the peak heights at  $+H_K^{\text{eff}}$  and  $-H_K^{\text{eff}}$  is visible for all samples. As previously discussed, these features indicate the presence of anisotropy dispersion in these samples rather than single-domain particulate nature with uniaxial anisotropy. For sample A, there is no significant difference between the peak positions in the TS isotherm for IP and OOP orientations of  $H_{DC}$ , indicating the almost equal contribution of the IP and OOP spin configurations. This observation is in good agreement with the IP and OOP  $M(H)$  hysteresis loops measured on this sample. A large hysteresis in the TS is also notable for both IP and OOP configurations, which is a clear manifestation of the asymmetric peak heights due to anisotropy dispersion. For sample B, the peak heights at  $\pm H_K^{\text{eff}}$  are almost symmetrical for the IP configuration in sharp contrast to the OOP configuration (the peak heights at  $\pm H_K^{\text{eff}}$  are identified as  $\pm d$ ). Hence, negligible hysteresis was observed for the IP configuration, whereas the hysteresis remains significant for the OOP configuration. On the other hand, the TS curve for sample C exhibits significant hysteresis for both IP and OOP orientations. Considering the unipolar field scan ( $+H_{DC}^{\text{sat}} \rightarrow -H_{DC}^{\text{sat}}$ ), the IP TS curve shows a very broad maximum at positive anisotropy, whereas the negative anisotropy peak is almost smeared out completely, which sig-

nifies very high anisotropy dispersion in the IP orientation. Most importantly, we noticed that the peaks in the TS isotherm occur at higher field values for the IP configuration in comparison to the OOP configuration for both samples B and C. It is to be noted that the maxima observed in the TS scans at  $\pm H_K^{\text{eff}}$  are associated with the contributions from the spins aligned orthogonal to the direction of  $H_{DC}$  [48]. In other words, for the IP configuration, the TS scans probe the dynamics of the OOP spins and vice versa. Hence, the positive peaks in the TS curves for the IP and OOP configurations are identified as the positive OOP effective anisotropy field  $+H_K^{\text{eff, OOP}} = +H_K^{OOP}$  and the positive IP effective anisotropy field  $+H_K^{\text{eff, IP}} = +H_K^{IP}$ , respectively. Hence,  $+H_K^{OOP} > +H_K^{IP}$  at  $T = 300$  K for both samples B and C, implying IP spin alignment. Conversely,  $+H_K^{IP} > +H_K^{OOP}$  for sample D at  $T = 300$  K validates our previous argument on the transition from IP to OOP magnetic anisotropy with increasing Gd concentration.

Since samples B and C show compensation within the measured temperature range, we chose to demonstrate the behavior of the IP and OOP TS curves close to their compensation points. In Figs. 7(e)–7(h), we compare the IP and OOP TS data for samples A–D, respectively, for bipolar field scans at  $T = 200$  K, which is the compensation temperature of sample C. In sharp contrast to the TS data observed at  $T = 300$  K

[see Fig. 8(a)–8(d)], we found that  $+H_K^{IP} > +H_K^{OOP}$  for all samples. However, the difference in the IP and OOP effective anisotropy fields  $\Delta H_K = (H_K^{IP} - H_K^{OOP})$  is higher in sample C than the rest of the samples. Another noticeable feature is that the peak heights at positive and negative anisotropy fields are nearly symmetric in the OOP TS curves for all samples, whereas the IP TS curves show slightly asymmetric peak heights for samples C and D that cause clear hysteresis between the  $+H_{DC}^{sat} \rightarrow -H_{DC}^{sat}$  and  $-H_{DC}^{sat} \rightarrow +H_{DC}^{sat}$  field scans. Similarly, in Figs. 7(i)–7(l), we compare the IP and OOP TS data for samples A–D, respectively, for bipolar field scans at  $T = 60$  K, which is close to the compensation temperature of sample B ( $T_{Comp} \approx 70$  K). As observed for  $T = 200$  K,  $+H_K^{IP} > +H_K^{OOP}$  for all samples, and  $\Delta H_K$  is higher in sample B than the rest of the samples. Unlike the TS data at  $T = 200$  K, considerable hysteresis is observed between the  $+H_{DC}^{sat} \rightarrow -H_{DC}^{sat}$  and  $-H_{DC}^{sat} \rightarrow +H_{DC}^{sat}$  field scans for the IP configurations for all samples. This implies anisotropy dispersion is also significant at low temperatures for all samples, especially for the IP orientation. For sample D, the negative anisotropy peak in the IP TS curve is fully smeared out for the  $+H_{DC}^{sat} \rightarrow -H_{DC}^{sat}$  field scan. Sample D exhibits an additional remarkable feature in the OOP TS curves at all temperatures: a sharp peak centering around the zero field for both  $+H_{DC}^{sat} \rightarrow -H_{DC}^{sat}$  and  $-H_{DC}^{sat} \rightarrow +H_{DC}^{sat}$  field scans. However, a closer view [see the inset of Fig. 7(l)] reveals the appearance of a peak at  $-H_{SW}$  ( $+H_{SW}$ ), while scanning the field from  $+H_{DC}^{sat}$  ( $-H_{DC}^{sat}$ )  $\rightarrow -H_{DC}^{sat}$  ( $+H_{DC}^{sat}$ ). This peak is possibly associated with the switching field. The absence of this feature at  $\pm H_{SW}$  for the IP configuration of this sample or both IP and OOP configurations in the other three samples may be because of the broad anisotropy peak which dominates and smears out the switching peak.

#### IV. DISCUSSION

To summarize the magnetic properties of  $Fe_{100-x}Gd_x$  films, we have made two important observations especially for samples B and C around their compensation points. First, as the compensation point is approached, a two-step magnetization reversal behavior starts appearing in the OOP  $M(H)$  loop a few Kelvins above and below the compensation temperature. Two-step magnetization reversal has also been observed in a recent study on amorphous FeGd films, where the high field switching was attributed to the Gd-enriched columnar domains with OOP anisotropy embedded in Fe-enriched domains with IP anisotropy formed due to partial Fe diffusion from the FeGd layer to the adjacent Ta layer [24]. Such a chemical phase segregation was observed for the films with thickness  $\geq 40$  nm, but it was absent for film thicknesses  $\leq 20$  nm. Chemical phase segregation in RE-TM-based amorphous films is not uncommon. For example, Stanciu *et al.* [49] recently reported the existence of nanoscale phase separation in amorphous  $Fe_{100-x}Gd_x$  thin films with thicknesses between 70 and 90 nm, particularly for the composition  $Fe_{79}Gd_{21}$ , which is close to the composition range  $22.8 \leq x \leq 26.2$  for our  $Fe_{100-x}Gd_x$  amorphous films with thicknesses  $\sim 80$ –90 nm. Moreover, by making use of magnetic force microscopy, Basumatary *et al.* [50] evidenced the presence of magnetically phase-separated regions in Tb-Fe amorphous films with strong PMA. The

thicknesses of all our films are also  $\approx 80$  nm; there is a possibility that our system is phase segregated into Fe- and Gd-rich regions with different orientations of local anisotropy axes. The two-steps in the OOP  $M(H)$  loop observed in samples B and C can thus be explained by sequential magnetization reversals of the Fe-enriched region with low coercivity and Gd-enriched region with higher coercivity. The absence of this behavior in the IP hysteresis loop is consistent with the OOP orientations of the Gd-enriched domains. Since the  $Fe_{100-x}Gd_x$  system undergoes a transformation from a high-temperature Fe-aligned state to a low-temperature Gd-aligned state, the Gd-enriched phase plays a dominating role in the vicinity of the compensation as well as at low temperatures. As the Gd-enriched phase prefers an OOP spin configuration, the effective magnetic easy axis also undergoes a transformation from an IP to an OOP configuration around the compensation, which indicates the occurrence of spin reorientation in both samples B and C. Increase in the OOP coercivity with increasing Gd concentration is consistent with OOP spin configuration of a Gd-enriched phase.

In addition to the two-step magnetization reversal, a second magnetization switching behavior accompanied by a minor hysteresis loop appears only within a narrow temperature window around the compensation temperature for samples B and C. In a ferrimagnet alloy such as  $Fe_{100-x}Gd_x$ , the complexity in the magnetic properties arises from the antiferromagnetic exchange coupling between the Fe and Gd sublattices, as well as the distinct temperature profiles of the individual sublattice magnetizations. Like antiferromagnets, it is energetically favorable for a ferrimagnet to align its magnetic easy axis perpendicular to the applied magnetic field. If the magnetic anisotropy is not very strong and a magnetic field is applied parallel to the magnetic easy axis, a competition between Zeeman energy and magnetic anisotropy energy causes a sudden rotation of the two sublattice magnetizations perpendicular to the direction of the applied magnetic field above a certain critical magnetic field. This causes a transformation of the system from an antiparallel collinear spin configuration to a noncollinear canted spin configuration above that critical field. This phenomenon is known as the SF transition, and  $\mu_0 H_{SF}$  represents the critical field for SF transition. As per our assumption, our  $Fe_{100-x}Gd_x$  system is chemically inhomogeneous and possibly phase segregates into Fe- and Gd-enriched regions. In this framework, we can visualize the SF transition as the flopping of the Fe- and Gd-enriched subnetworks rather than considering the flopping of individual Fe and Gd sublattices distributed homogeneously throughout the system. According to the two-sublattice model, the resultant saturation magnetization of our ferrimagnetic system at any temperature  $T$  can thus be expressed as  $M_S = (M_{Gd}^{Rich} - M_{Fe}^{Rich})$ , where  $M_{Gd}^{Rich}$  and  $M_{Fe}^{Rich}$  are the saturation magnetizations of the Fe- and Gd-enriched subnetworks, respectively. A collinear antiparallel configuration of the sublattice magnetizations persists up to a certain critical value of the external magnetic field  $H_{DC} = H_{C,1} = \lambda_{Gd-Fe}^{inh}(M_{Gd}^{Rich} - M_{Fe}^{Rich})$ , where  $\lambda_{Gd-Fe}^{inh}$  is the molecular field constant associated with the exchange interaction between Fe- and Gd-enriched subnetworks [51,52]. For  $H_{DC} \geq H_{C,1}$ , the system switches to the SF state that persists in the field range  $H_{C,1} \leq H_{DC} \leq H_{C,2}$ . A field-induced transformation from the noncollinear canted

configuration to a collinear parallel configuration takes place as the applied magnetic field exceeds a second critical field  $H_{DC} \geq H_{C,2} = \lambda_{Gd-Fe}^{inh}(M_{Gd}^{Rich} - M_{Fe}^{Rich})$  [51,52]. Typically, the values of the critical fields  $H_{C,1}$  and  $H_{C,2}$  lie in the range of  $\sim 10$ –100 T. However, at temperatures close to the compensation point,  $H_{C,1}$  and  $H_{C,2}$  become small, and the difference between the critical fields ( $H_{C,1} - H_{C,2}$ ) also become narrow [51,52]. Clearly,  $H_{C,1} = 0$  at  $T = T_{Comp}$ , indicating the appearance of the canted noncollinear state at a much lower field at the compensation temperature. This explains the appearance of the sudden magnetization reversal behavior at  $\mu_0 H_{SF}$  in both samples B and C in the vicinity of their compensation points. While decreasing the field from  $H_{DC} \geq H_{C,2}$ , the transformation from collinear parallel spin configuration to canted SF state occurs at  $\approx H_{C,2}^* < H_{C,2}$ , and upon further decreasing the field, the antiparallel collinear spin configuration is retrieved at  $\approx H_{C,1}^* < H_{C,1}$ , giving rise to a hysteresis around  $\mu_0 H_{SF}$  [53]. Since the field-induced transition from the collinear antiparallel state to the noncollinear SF state is a first-order metamagnetic transition, such hysteresis is expected [53,54]. It was shown that  $H_{C,1}$  and  $H_{C,1}^*$  are related to the exchange field  $H_E$  and anisotropy field  $H_K$  at  $T = 0$  K through the relation [53,55,56]

$$H_{C,1}^* = \left( \frac{2H_E - H_K}{2H_E + H_K} \right) H_{C,1}. \quad (4)$$

Equation (4) indicates that  $H_{C,1} > H_{C,1}^*$ , which explains the occurrence of a minor hysteresis loop observed around the SF transition in samples B and C in the vicinity of the compensation point. Thermodynamically, the SF transition field is defined as  $H_{SF} = \sqrt{(H_{C,1} H_{C,1}^*)}$  [53]. The difference ( $H_{C,1} - H_{C,1}^*$ ) decreases with increasing temperature. For better visibility of the critical fields, we show the expanded OOP  $M(H)$  loop for sample B at  $T = 75$  K in Fig. 4(c). The values of  $\mu_0 H_{C,1}$ ,  $\mu_0 H_{C,2}$ ,  $\mu_0 H_{C,1}^*$ , and  $\mu_0 H_{C,2}^*$  are 0.83, 0.91, 0.63, and 0.73 T, respectively, and hence, the correct value of  $\mu_0 H_{SF} = 0.73$  T for sample B at  $T = 75$  K. Similarly, the values of  $\mu_0 H_{C,1}$ ,  $\mu_0 H_{C,2}$ ,  $\mu_0 H_{C,1}^*$ ,  $\mu_0 H_{C,2}^*$ , and  $\mu_0 H_{SF}$  are 1.13, 1.22, 0.98, 1.08, and 1.05 T, respectively at  $T = 100$  K.

Next, we discuss the difference between the IP and OOP saturation magnetizations for our  $Fe_{100-x}Gd_x$  films. As we can see from the insets of Fig. 2, the difference between the IP and OOP saturation magnetizations is small at low fields, whereas the difference increases at higher fields. Krupinski *et al.* [41] also observed similar increase in difference between the IP and OOP magnetization values above the low-field ferrimagnetic saturation in FeGd amorphous films. Significant difference in the IP and OOP saturation magnetizations has also been observed in other RE-TM-based amorphous ferrimagnetic films [50,57,58]. We believe that the origin of such a difference in saturation magnetization value between IP and OOP configurations is related to the SF transition, as discussed in the previous section. Below the SF transition, even if the  $M(H)$  loop shows tendency of saturation, it is not the complete saturation but rather the ferrimagnetic macrospin saturation. A very high field ( $\sim 10$ –100 T) is needed to achieve complete saturation where the RE and TM moments are completely aligned [59]. To visualize the entire picture as a function of field, let us consider the “rigid rotation model” for two sublattices in a RE-TM-based ferrimagnet [60]. Under

the application of a nonzero field (much lower than  $H_{C,1}$ ), the RE and TM sublattice magnetizations are not perfectly antiferromagnetically aligned [60], rather they deviate from the antiparallel alignment by a small angle because of the competition between the Zeeman energy, the exchange energy, and the anisotropy energy associated with individual elements. Thus, the macrospin consisting of the RE and TM sublattice magnetizations forms a rigid spin configuration with a very small canting angle, where the canting angle depends on the local anisotropy. When the applied field exceeds  $H_{C,1}$ , the system transforms from the rigid canted/nearly antiparallel state into the SF state with a larger canting angle between the RE and TM sublattices, and for an applied field  $\geq H_{C,2}$ , both sublattice magnetizations reorient toward the applied field direction, and hence, a complete saturation/alignment takes place. Now let us consider phase segregation as a small perturbation to this scenario. Since there is a possibility that our system is phase segregated into Fe- and Gd-rich regions with different orientations of local anisotropy axes, and hence, the canting angles of the rigid ( $M_{Gd}^{Rich} + M_{Fe}^{Rich}$ ) macrospins are different for different phase-segregated regions for applied fields  $\leq H_{C,1}$ . This is possibly the origin of the different values of the ferrimagnetic macrospin saturation magnetization values for the IP and OOP configurations for our FeGd system when the applied field is smaller than  $H_{C,1}$  or  $H_{C,2}$ .

The disappearance of the two-step magnetization reversals around the compensation point is expected as the Fe- and Gd-enriched subnetwork magnetizations cancel each other and undergo a transformation to a canted SF state first before flipping their directions simultaneously parallel to the applied field direction rather than independent reversals. Magnetic compensation also strongly influences both squareness of the OOP  $M(H)$  loop and coercive force, especially in samples B and C. Thus, it seems that magnetic anisotropy plays a crucial role in controlling the magnetic properties of this system, specifically around the compensation temperature. As there may be chemically phase-segregated regions, these phases have different easy axes which lead to a competition between local anisotropies and the Zeeman energies, particularly around the global compensation temperature ( $T_{Comp}$ ). Hence, it is imperative to have a clear understanding of the effective magnetic anisotropy fields as a function of temperature to elucidate the complex magnetic behavior observed in these films around the compensation.

As we already mentioned, the TS scans probe the dynamics of the OOP spins for the IP configuration and vice versa. From our TS measurements, we observed that the effective anisotropy field is higher for the OOP configurations than the IP configurations, i.e.,  $+H_K^{IP}(T) > +H_K^{OOP}(T)$  below the spin reorientation transition ( $T_{SR}$ ) for samples B and C and throughout the measured temperature range for sample D. Thus, our TS data are consistent with our magnetometry data. On the other hand, we observed multiple spin reorientation transitions for sample A. Such complex temperature dependence of  $+H_K^{IP}$  and  $+H_K^{OOP}$  suggest that there is strong competition between the IP and OOP anisotropies in the system. As discussed earlier, for simplicity, we can consider our  $Fe_{100-x}Gd_x$  system to be composed of two different anisotropy phases: (1) the Gd-enriched phase which prefers OOP anisotropy and (2) the Fe-enriched phase that prefers

IP anisotropy. The two-step reversal behavior observed in the OOP  $M(H)$  at low temperatures indicated the development of the OOP spin configuration in the Gd-enriched phase. Hence, a strong competition between the anisotropies of the Gd- and Fe-enriched regions is expected. Such competing magnetic anisotropies can give rise to anisotropy crossover(s) depending on the dominant contribution, resulting in spin reorientation(s) in the system. Moreover, assuming that our system is most likely phase segregated into Fe- and Gd-enriched regions, we can expect that different regions have distinct preferred orientations of the magnetic easy axes. Our TS measurements probe the effective anisotropy field which is certainly the average of all local anisotropy axes. This is the origin of anisotropy dispersion in the  $\text{Fe}_{100-x}\text{Gd}_x$  system which leads to the observed asymmetry in the peak heights at  $+H_K^{\text{eff}}$  and  $-H_K^{\text{eff}}$  as well as broadened peak in the bipolar TS curves for most of the samples shown in Fig. 7.

It is known that the RF TS is the low-frequency limit of the ferromagnetic resonance (FMR) [61], and thus, its dynamics follows the Landau-Lifshitz-Gilbert equation [62]. In the case of FMR, the field dependence of dynamic susceptibility is well described by the Lorentzian function [63], and hence, the line shapes for the TS curves can also be described by the Lorentzian function, which is expressed as

$$\frac{\Delta\chi_T}{\chi_T} = A \frac{\left(\frac{\Delta H}{2}\right)^2}{(H_{\text{DC}} - H_K^{\text{eff}})^2 + \left(\frac{\Delta H}{2}\right)^2}, \quad (5)$$

where  $A$  is the proportionality constant, and  $\Delta H$  is the line width of the TS curves. Like FMR, the symmetry of the TS line shape may also depend on the relative phase between RF electric and magnetic field components. When a plane electromagnetic (EM) wave travels through free space, the electric and magnetic field vectors associated with the EM wave are in phase. However, if the EM wave enters a metallic medium, the electric and magnetic field vectors of the RF wave become out of phase. Since our FeGd system is metallic, the magnetic and electric field vectors associated with the RF EM wave generated by the inductor coil may also become out of phase inside the sample. In such a case, the resultant TS line shape can be considered as a linear combination of symmetric and antisymmetric Lorentzian functions, where the symmetric and antisymmetric Lorentzian functions account for the in-phase and out-of-phase components of the RF wave [64]. To determine the effective anisotropy field from our field-dependent TS curves, we fitted the line shapes for the TS curves with the following expression [64]:

$$\frac{\Delta\chi_T}{\chi_T} = \chi_{\text{Sym}} \frac{\left(\frac{\Delta H}{2}\right)^2}{(H_{\text{DC}} - H_K^{\text{eff}})^2 + \left(\frac{\Delta H}{2}\right)^2} + \chi_{\text{Asym}} \frac{\frac{\Delta H}{2}(H_{\text{DC}} - H_K^{\text{eff}})}{(H_{\text{DC}} - H_K^{\text{eff}})^2 + \left(\frac{\Delta H}{2}\right)^2} + \chi_0, \quad (6)$$

where  $\chi_{\text{Sym}}$  and  $\chi_{\text{Asym}}$  are the coefficients of symmetric and antisymmetric Lorentzian functions, and  $\chi_0$  is the constant offset parameter. Figures 8(a)–8(d) demonstrate the fit of the unipolar TS curves using Eq. (6) for sample B at two selected temperatures for both IP and OOP configurations. It is evident

that asymmetric contribution (asymmetry in the TS curve with respect to  $\pm H_K^{\text{eff}}$  in the field range between 0 and  $\pm H_{\text{DC}}^{\text{sat}}$ ) is more pronounced for the IP configuration at  $T = 300$  K.

Next, we concentrate on the temperature dependence of  $+H_K^{\text{IP}}$  and  $+H_K^{\text{OOP}}$ , which we have associated with the effective anisotropy fields for the OOP and IP configurations obtained from the Lorentzian fits. Figures 8(e)–8(h) compare the temperature dependence of  $+H_K^{\text{OOP}}$  and  $+H_K^{\text{IP}}$  for samples A–D, respectively, in the temperature range  $40\text{ K} \leq T \leq 300\text{ K}$ , where  $+H_K^{\text{OOP}}$  and  $+H_K^{\text{IP}}$  are represented by a solid red sphere and solid blue square, respectively. Complex temperature dependences of the IP and OOP effective anisotropy fields are noticeable for different samples. For sample A, the temperature dependences of both  $+H_K^{\text{OOP}}$  [ $+H_K^{\text{OOP}}(T)$ ] and  $+H_K^{\text{IP}}$  [ $+H_K^{\text{IP}}(T)$ ] follow almost the same trend: decrease from  $T = 300$  K, followed by a broad maximum, and then again decrease with further reducing the temperature. Because of different magnitudes of  $+H_K^{\text{IP}}$  and  $+H_K^{\text{OOP}}$  at different temperatures, there are some crossovers. In the temperature range  $400\text{ K} \leq T \leq 300\text{ K}$ , there are three crossovers at  $T_{\text{SR1}}$ ,  $T_{\text{SR2}}$ , and  $T_{\text{SR3}}$ , which are indicated by arrows. For  $T > T_{\text{SR1}}$ ,  $+H_K^{\text{OOP}} \geq +H_K^{\text{IP}}$ , whereas  $+H_K^{\text{OOP}} < +H_K^{\text{IP}}$  in the temperature range  $T_{\text{SR1}} \leq T \leq T_{\text{SR2}}$ , and again,  $+H_K^{\text{OOP}} > +H_K^{\text{IP}}$  for  $T_{\text{SR2}} \leq T \leq T_{\text{SR3}}$ . Below the third crossover at  $T_{\text{SR3}}$ ,  $+H_K^{\text{IP}} > +H_K^{\text{OOP}}$  down to the lowest temperature.

Unlike the multiple spin reconfigurations in sample A, there is only one anisotropy crossover at  $T = T_{\text{SR}}$  in the temperature range  $40\text{ K} \leq T \leq 300\text{ K}$  for both samples B and C. For both samples B and C,  $+H_K^{\text{OOP}} > +H_K^{\text{IP}}$  for  $T \geq T_{\text{SR}}$ , but below the spin reorientation,  $+H_K^{\text{IP}} > +H_K^{\text{OOP}}$  down to the lowest temperature. Thus, these samples transform from a high-temperature IP anisotropy-dominated state to a low-temperature OOP anisotropy-dominated state below the spin reorientation transition. This is also in good agreement with our magnetometry data. There is another important feature: for sample B, both  $+H_K^{\text{OOP}}(T)$  and  $+H_K^{\text{IP}}(T)$  undergo an abrupt decrease  $< 150\text{ K}$  and exhibit a broad minimum in the vicinity of its compensation temperature ( $\approx 70\text{ K}$ ). This feature around the compensation point is stronger in  $+H_K^{\text{IP}}(T)$  than in  $+H_K^{\text{OOP}}(T)$ . On the other hand, for sample C,  $+H_K^{\text{IP}}(T)$  shows a prominent dip, but  $+H_K^{\text{OOP}}(T)$  shows a slope change around the compensation ( $\approx 200\text{ K}$ ). At lower temperatures,  $+H_K^{\text{IP}}(T)$  increases almost linearly and shows a broad hump  $\sim 100\text{ K}$ , and  $+H_K^{\text{OOP}}(T)$  shows a broad minimum just below the compensation, which is followed by a slight increase and then remains almost unaltered down to the lowest temperature. Unlike samples A–C, sample D does not show any spin reorientation in the measured temperature window and  $+H_K^{\text{IP}} > +H_K^{\text{OOP}}$  at all temperatures. Moreover, both  $+H_K^{\text{OOP}}(T)$  and  $+H_K^{\text{IP}}(T)$  exhibit a broad maximum at  $\approx 150\text{ K}$ .

To explain the anomalous behavior of  $H_K^{\text{IP}}(T)$  and  $H_K^{\text{OOP}}(T)$  in the vicinity of  $T_{\text{Comp}}$ , let us start from the energy landscape of the system. For simplicity, we consider that the  $\text{Fe}_{100-x}\text{Gd}_x$  system is composed of Gd- and Fe-enriched phases which are antiferromagnetically coupled by intersubnetwork exchange interaction. A schematic representation of different orientations of the subnetwork magnetizations associated with the Gd-enriched ( $M_{\text{Gd}}^{\text{Rich}}$ ) and Fe-enriched ( $M_{\text{Fe}}^{\text{Rich}}$ ) domains relative to the applied bias field ( $H_{\text{DC}}$ ) is shown in

Fig. 6(c). In the absence of  $H_{DC}$ , both  $M_{Gd}^{\text{Rich}}$  and  $M_{Fe}^{\text{Rich}}$  prefer an antiparallel alignment along the magnetic easy axis. When  $H_{DC}$  is applied at an angle  $\phi$  with respect to the easy axis, both  $M_{Gd}^{\text{Rich}}$  and  $M_{Fe}^{\text{Rich}}$  undergo slight deviation from the antiparallel alignment by angles  $\theta_{Gd}$  and  $\theta_{Fe}$ , respectively. Since the Gd moment dominates at low temperatures, we assume that  $M_{Gd}^{\text{Rich}} > M_{Fe}^{\text{Rich}}$ . In the framework of the mean-field model, the energy density for this ferrimagnetic system can be expressed as [60,65]

$$E = [-\mu_0 H_{DC} M_{Gd}^{\text{Rich}} \cos(\phi - \theta_{Gd}) + \mu_0 H_{DC} M_{Fe}^{\text{Rich}} \cos(\phi - \theta_{Fe})]$$

$$K_{\text{eff}} = M_S^2 \left\{ \frac{\lambda_{Gd-Fe}^{\text{inh}} M_{Gd}^{\text{Rich}} M_{Fe}^{\text{Rich}} (K_1^{\text{Gd}} + K_1^{\text{Fe}}) + 2K_1^{\text{Gd}} K_1^{\text{Fe}}}{2 \left[ K_1^{\text{Gd}} (M_{Fe}^{\text{Rich}})^2 + K_1^{\text{Fe}} (M_{Gd}^{\text{Rich}})^2 \right] + \lambda_{Gd-Fe}^{\text{inh}} M_{Gd}^{\text{Rich}} M_{Fe}^{\text{Rich}} M_S^2} \right\}. \quad (8)$$

Here,  $M_S = (M_{Gd}^{\text{Rich}} - M_{Fe}^{\text{Rich}})$  is the net magnetization of the  $\text{Fe}_{100-x}\text{Gd}_x$  system. Equation (8) suggests that  $K_{\text{eff}}$  is strongly dependent on the sublattice magnetizations, sublattice anisotropies, and intersublattice exchange interaction. Most importantly, Eq. (8) indicates that  $K_{\text{eff}}$  becomes zero at the compensation point, as  $M_S = (M_{Gd}^{\text{Rich}} - M_{Fe}^{\text{Rich}}) = 0$ , which explains the minimum/dip observed in  $H_K^{\text{OOP}}(T)$  and  $+H_K^{\text{IP}}(T)$  at  $T_{\text{Comp}}$  for both samples B and C. The minimum in the effective anisotropy constant/field around  $T_{\text{Comp}}$  is expected in RE-TM-based compensated ferrimagnets [60,65–67], which is generally explained in terms of canting of the sublattice magnetizations near  $T_{\text{Comp}}$ .

Finally, it is known that the microstructure and, hence, the internal planar stress in physical vapor deposited/sputtered films are sensitive to the deposition conditions, e.g., the partial pressure of Ar ( $P_{\text{Ar}}$ ) [68,69]. The orientation of the magnetic easy axis strongly depends on the internal stress of the film and, hence, is dependent on the Ar partial pressure. For FeGd amorphous films, it is reported that the internal planar stress is compressive at  $P_{\text{Ar}} = 6 \times 10^{-2}$  Torr, which transforms to tensile at  $P_{\text{Ar}} = 10 \times 10^{-2}$  Torr [69]. Nevertheless, PMA is significant for the films with compressive strain. This internal stress-induced PMA can be avoided by using a lower Ar partial pressure during deposition. The Ar partial pressure during the deposition of our FeGd films was  $6 \times 10^3$  Torr, which is almost an order of magnitude lower than that for the films with compressive strain. Moreover, influence of internal stress on the uniaxial anisotropy is the minimum for the Gd atomic percent range  $22 \leq x \leq 28$  [69], and in this paper, we are dealing with the composition range  $22.8 \leq x \leq 26.2$  in  $\text{Fe}_{100-x}\text{Gd}_x$ . Thus, the stress-induced anisotropy in our  $\text{Fe}_{100-x}\text{Gd}_x$  films is negligible, and the origin of PMA observed in these films is intrinsic. This paper concerns the precise determination of effective anisotropy fields as a function of temperature using the TS technique for both IP and OOP configurations among the RE-TM-based systems, and our TS technique would pave the way for the development of spintronic devices with excellent PMA.

$$+ (K_1^{\text{Gd}} \sin^2 \theta_{Gd} + K_1^{\text{Fe}} \sin^2 \theta_{Fe}) \\ - [\lambda_{Gd-Fe}^{\text{inh}} M_{Gd}^{\text{Rich}} M_{Fe}^{\text{Rich}} \cos(\theta_{Gd} - \theta_{Fe})], \quad (7)$$

where  $K_1^{\text{Gd}}$  and  $K_1^{\text{Fe}}$  are the first-order anisotropy constants associated with the Gd- and Fe-enriched phases, respectively, and  $\lambda_{Gd-Fe}^{\text{inh}}$  is the intersubnetwork Weiss field constant. In Eq. (7), the first and second, third, and fourth terms represent the Zeeman energy, the anisotropy energy, and the intersublattice exchange energy. Following the approach of Sarkis and Callen [60] and Drzazga and Drzazga [65], the effective anisotropy constant for our compensated ferrimagnetic  $\text{Fe}_{100-x}\text{Gd}_x$  system can be expressed as

## V. CONCLUSIONS

In summary, we have used the DC magnetometry and RF TS measurements to carefully examine the temperature evolution of IP and OOP effective anisotropy fields in ferrimagnetic  $\text{Fe}_{100-x}\text{Gd}_x$  amorphous films by varying the Gd concentration. The compensation temperature moves to a higher temperature with increasing Gd concentration. We suggest that the  $\text{Fe}_{100-x}\text{Gd}_x$  system is phase segregated into Fe- and Gd-enriched regions. A two-step reversal behavior emerges in the OOP  $M(H)$  loop near compensation, which we attribute to the sequential magnetization reversals of Fe- and Gd-enriched domains. Since the Gd-enriched domains prefer OOP anisotropy, this two-step magnetization reversal suggests a temperature-induced transformation from IP to OOP spin configuration below a certain temperature. Our RF TS measurements indicate that the effective magnetic anisotropy for the OOP configuration dominates over the IP configuration (i.e.,  $H_K^{\text{IP}} > H_K^{\text{OOP}}$ ) below a certain temperature, which validates the occurrence of spin reorientation. Both IP and OOP anisotropy fields determined from our TS measurement exhibit a minimum around the compensation, which has been supported by the SW model. Thus, the presence of competing magnetic anisotropies and spin reorientations, as revealed by our TS data, together with the magnetometry results potentially point toward the existence of phase-separated regions with distinct magnetic easy axes in our amorphous ferrimagnetic  $\text{Fe}_{100-x}\text{Gd}_x$  films.

## ACKNOWLEDGMENTS

H.S. acknowledges support from USF Department of Energy, Office of Basic Energy Sciences, Division of Materials Science and Engineering under Award No. DE-FG02-07ER46438. J.E.S. and D.A.A. acknowledge support of the National Science Foundation under Grant No. ECCS-1952957.

[1] P. Hansen, C. Clausen, G. Much, M. Rosenkranz, and K. Witter, *J. Appl. Phys.* **66**, 756 (1989).

[2] S. Mangin, M. Gottwald, C. Lambert, D. Steil, V. Uhlíř, L. Pang, M. Hehn, S. Alebrand, M. Cinchetti, and G. Malinowski, *Nat. Mater.* **13**, 286 (2014).

[3] L. Le Guyader, S. El Moussaoui, M. Buzzi, M. Savoini, A. Tsukamoto, A. Itoh, A. Kirilyuk, T. Rasing, F. Nolting, and A. V. Kimel, *Phys. Rev. B* **93**, 134402 (2016).

[4] B. Dai, T. Kato, S. Iwata, and S. Tsunashima, *IEEE Trans. Magn.* **48**, 3223 (2012).

[5] T. Ostler, J. Barker, R. Evans, R. Chantrell, U. Atxitia, O. Chubykalo-Fesenko, S. El Moussaoui, L. Le Guyader, E. Mengotti, and L. Heyderman, *Nat. Commun.* **3**, 666 (2012).

[6] P. Hansen, *J. Appl. Phys.* **63**, 2364 (1988).

[7] N. Roschewsky, C.-H. Lambert, and S. Salahuddin, *Phys. Rev. B* **96**, 064406 (2017).

[8] R. Mishra, J. Yu, X. Qiu, M. Motapothula, T. Venkatesan, and H. Yang, *Phys. Rev. Lett.* **118**, 167201 (2017).

[9] J. Kim, D. Lee, K.-J. Lee, B.-K. Ju, H. C. Koo, B.-C. Min, and O. Lee, *Sci. Rep.* **8**, 6017 (2018).

[10] Z. Zheng, Y. Zhang, X. Feng, K. Zhang, J. Nan, Z. Zhang, G. Wang, J. Wang, N. Lei, D. Liu, Y. Zhang, and W. Zhao, *Phys. Rev. Appl.* **12**, 044032 (2019).

[11] R. Schneider, M. Fix, J. Bensmann, S. Michaelis de Vasconcellos, M. Albrecht, and R. Bratschitsch, *Appl. Phys. Lett.* **115**, 152401 (2019).

[12] L. Caretta, M. Mann, F. Büttner, K. Ueda, B. Pfau, C. M. Günther, P. Hessing, A. Churikova, C. Klose, and M. Schneider, *Nat. Nanotechnol.* **13**, 1154 (2018).

[13] S. Woo, K. M. Song, X. Zhang, Y. Zhou, M. Ezawa, X. Liu, S. Finizio, J. Raabe, N. J. Lee, and S.-I. Kim, *Nat. Commun.* **9**, 959 (2018).

[14] R. C. Taylor and A. Gangulee, *Phys. Rev. B* **22**, 1320 (1980).

[15] T. A. Ostler, R. F. L. Evans, R. W. Chantrell, U. Atxitia, O. Chubykalo-Fesenko, I. Radu, R. Abrudan, F. Radu, A. Tsukamoto, A. Itoh, A. Kirilyuk, T. Rasing, and A. Kimel, *Phys. Rev. B* **84**, 024407 (2011).

[16] R. Taylor and A. Gangulee, *J. Appl. Phys.* **48**, 358 (1977).

[17] R. E. Camley, *Phys. Rev. B* **35**, 3608 (1987).

[18] W. He, H.-L. Liu, H.-Y. Wu, J.-W. Cai, and Z.-H. Cheng, *Appl. Phys. Lett.* **106**, 042401 (2015).

[19] Y. Suzuki, S. Takayama, F. Kirino, and N. Ohta, *IEEE Trans. Magn.* **23**, 2275 (1987).

[20] W. Meiklejohn, *J. Appl. Phys.* **33**, 1328 (1962).

[21] H. Fu and M. Mansuripur, *Phys. Rev. B* **45**, 7188 (1992).

[22] H. Fu, M. Mansuripur, and P. Meystre, *Phys. Rev. Lett.* **66**, 1086 (1991).

[23] V. G. Harris, K. D. Aylesworth, B. N. Das, W. T. Elam, and N. C. Koon, *Phys. Rev. Lett.* **69**, 1939 (1992).

[24] E. Kirk, C. Bull, S. Finizio, H. Sepehri-Amin, S. Wintz, A. K. Suszka, N. S. Bingham, P. Warnicke, K. Hono, P. W. Nutter, J. Raabe, G. Hrkac, T. Thomson, and L. J. Heyderman, *Phys. Rev. Mater.* **4**, 074403 (2020).

[25] M. Urner-Wille and K. Witter, *J. Magn. Magn. Mater.* **13**, 77 (1979).

[26] Y. Mimura, N. Imamura, and T. Kobayashi, *J. Appl. Phys.* **47**, 368 (1976).

[27] E. Jesenská, T. Ishibashi, L. Beran, M. Pavelka, J. Hamrle, R. Antoš, J. Zázvorka, and M. Veis, *Sci. Rep.* **9**, 16547 (2019).

[28] J. Coey, *J. Appl. Phys.* **49**, 1646 (1978).

[29] S. Ohbayashi, M. Harada, M. Nawate, M. Ohkoshi, S. Honda, and T. Kusuda, *IEEE Transl. J. Magn. Jpn.* **2**, 340 (1987).

[30] J. Orehovsky and K. Schröder, *J. Appl. Phys.* **43**, 2413 (1972).

[31] T. Morishita, Y. Togami, and K. Tsushima, *J. Phys. Soc. Jpn.* **54**, 37 (1985).

[32] Y. Mimura, N. Imamura, T. Kobayashi, A. Okada, and Y. Kushiro, *J. Appl. Phys.* **49**, 1208 (1978).

[33] Y. Choi, D. Haskel, A. Cady, J. C. Lang, D. R. Lee, G. Srager, J. S. Jiang, and S. D. Bader, *Phys. Rev. B* **73**, 174401 (2006).

[34] A. Drovosekov, A. Savitsky, D. Kholin, N. Kreines, V. Proglyado, M. Makarova, E. Kravtsov, and V. Ustinov, *J. Magn. Magn. Mater.* **475**, 668 (2019).

[35] R. E. Camley and D. R. Tilley, *Phys. Rev. B* **37**, 3413 (1988).

[36] K. Takanashi, Y. Kamiguchi, H. Fujimori, and M. Motokawa, *J. Phys. Soc. Jpn.* **61**, 3721 (1992).

[37] K. Okamoto and N. Miura, *Physica B* **155**, 259 (1989).

[38] O. Inyang, A. Rafiq, C. Swindells, S. Ali, and D. Atkinson, *Sci. Rep.* **10**, 9767 (2020).

[39] S. Mondal, A. Talapatra, J. Arout Chelvane, J. R. Mohanty, and A. Barman, *Phys. Rev. B* **100**, 054436 (2019).

[40] A. Talapatra, J. A. Chelvane, and J. Mohanty, *J. Magn. Magn. Mater.* **448**, 360 (2018).

[41] M. Krupinski, J. Hintermayr, P. Sobieszczyk, and M. Albrecht, *Phys. Rev. Mater.* **5**, 024405 (2021).

[42] See Supplemental Material at <http://link.aps.org/supplemental/10.1103/PhysRevB.104.094404> for x-ray reflectivity and high-angle x-ray diffraction data.

[43] A. Drovosekov, N. Kreines, A. Savitsky, E. Kravtsov, D. Blagodatkov, M. Ryabukhina, M. Milyaev, V. Ustinov, E. Pashaev, and I. Subbotin, *J. Experiment. Theoret. Phys.* **120**, 1041 (2015).

[44] H. Srikanth, J. Wiggins, and H. Rees, *Rev. Sci. Instrum.* **70**, 3097 (1999).

[45] A. Aharoni, E. H. Frei, S. Shtrikman, and D. Treves, *Bull. Res. Counc. Israel* **6**, 215 (1957).

[46] A. Hoare, R. Chantrell, W. Schmitt, and A. Eiling, *J. Phys. D: Appl. Phys.* **26**, 461 (1993).

[47] R. Matarranz, M. Contreras, G. Pan, B. Presa, J. Corrales, and J. Calleja, *J. Appl. Phys.* **99**, 08Q504 (2006).

[48] R. P. Madhogaria, C.-M. Hung, B. Muchharla, A. T. Duong, R. Das, P. T. Huy, S. Cho, S. Witanachchi, H. Srikanth, and M.-H. Phan, *Phys. Rev. B* **103**, 184423 (2021).

[49] A. Stanciu, G. Schinteie, A. Kuncser, N. Iacob, L. Trupina, I. Ionita, O. Crisan, and V. Kuncser, *J. Magn. Magn. Mater.* **498**, 166173 (2020).

[50] H. Basumatary, J. A. Chelvane, D. S. Rao, A. Talapatra, J. Mohanty, D. Kumar, V. Singh, S. Kamat, and R. Ranjan, *J. Alloys Compd.* **869**, 159571 (2021).

[51] A. E. Clark and E. Callen, *J. Appl. Phys.* **39**, 5972 (1968).

[52] A. Drovosekov, D. Kholin, and N. Kreines, *J. Experiment. Theoret. Phys.* **131**, 149 (2020).

[53] A. Paduan-Filho, C. C. Becerra, and F. Palacio, *Phys. Rev. B* **43**, 11107 (1991).

[54] M. Date and K. Nagata, *J. Appl. Phys.* **34**, 1038 (1963).

[55] F. B. Anderson and H. B. Callen, *Phys. Rev.* **136**, A1068 (1964).

[56] F. Keffer and H. Chow, *Phys. Rev. Lett.* **31**, 1061 (1973).

[57] K. Umadevi, S. Bysakh, J. A. Chelvane, S. Kamat, and V. Jayalakshmi, *J. Alloys Compd.* **663**, 430 (2016).

[58] A. Talapatra, J. A. Chelvane, B. Satpati, S. Kumar, and J. Mohanty, *J. Alloys Compd.* **774**, 1059 (2019).

[59] J. Becker, A. Tsukamoto, A. Kirilyuk, J. C. Maan, Th. Rasing, P. C. M. Christianen, and A. V. Kimel, *Phys. Rev. Lett.* **118**, 117203 (2017).

[60] A. Sarkis and E. Callen, *Phys. Rev. B* **26**, 3870 (1982).

[61] L. Spinu, I. Dumitru, A. Stancu, and D. Cimpoesu, *J. Magn. Magn. Mater.* **296**, 1 (2006).

[62] D. Cimpoesu, A. Stancu, and L. Spinu, *Phys. Rev. B* **76**, 054409 (2007).

[63] V. A. Ivanshin, J. Deisenhofer, H.-A. Krug von Nidda, A. Loidl, A. A. Mukhin, A. M. Balbashov, and M. V. Eremin, *Phys. Rev. B* **61**, 6213 (2000).

[64] M. Harder, Z. X. Cao, Y. S. Gui, X. L. Fan, and C.-M. Hu, *Phys. Rev. B* **84**, 054423 (2011).

[65] Z. Drzazga and M. Drzazga, *J. Magn. Magn. Mater.* **65**, 21 (1987).

[66] A. Ermolenko, *IEEE Trans. Magn.* **12**, 992 (1976).

[67] Z. Drzazga, *Physica B+C* **130**, 305 (1985).

[68] J. A. Thornton and D. Hoffman, *Thin Solid Films* **171**, 5 (1989).

[69] H. Takagi, S. Tsunashima, S. Uchiyama, and T. Fujii, *J. Appl. Phys.* **50**, 1642 (1979).